

Analytical propagation of errors in dynamic SPECT: estimators, degrading factors, bias and noise

Dan J Kadmas[†], Edward V R DiBella[†], Ronald H Huesman[‡] and Grant T Gullberg[†]

[†] Medical Imaging Research Laboratory, Department of Radiology, University of Utah, CAMT, 729 Arapen Drive, Salt Lake City, UT 84108-1218, USA

[‡] Center for Functional Imaging, Lawrence Berkeley National Laboratory, University of California, Berkeley, CA 94720, USA

E-mail: kadmas@mir1.med.utah.edu

Received 4 March 1999, in final form 6 May 1999

Abstract. Dynamic SPECT is a relatively new technique that may potentially benefit many imaging applications. Though similar to dynamic PET, the accuracy and precision of dynamic SPECT parameter estimates are degraded by factors that differ from those encountered in PET. In this work we formulate a methodology for analytically studying the propagation of errors from dynamic projection data to kinetic parameter estimates. This methodology is used to study the relationships between reconstruction estimators, image degrading factors, bias and statistical noise for the application of dynamic cardiac imaging with ^{99m}Tc-teboroxime. Dynamic data were simulated for a torso phantom, and the effects of attenuation, detector response and scatter were successively included to produce several data sets. The data were reconstructed to obtain both weighted and unweighted least squares solutions, and the kinetic rate parameters for a two-compartment model were estimated. The expected values and standard deviations describing the statistical distribution of parameters that would be estimated from noisy data were calculated analytically. The results of this analysis present several interesting implications for dynamic SPECT. Statistically weighted estimators performed only marginally better than unweighted ones, implying that more computationally efficient unweighted estimators may be appropriate. This also suggests that it may be beneficial to focus future research efforts upon regularization methods with beneficial bias–variance trade-offs. Other aspects of the study describe the fundamental limits of the bias–variance trade-off regarding physical degrading factors and their compensation. The results characterize the effects of attenuation, detector response and scatter, and they are intended to guide future research into dynamic SPECT reconstruction and compensation methods.

1. Introduction

Dynamic functional imaging using positron emission tomography (PET) and compartmental modelling is a well established methodology. More recently, developments in single-photon emission computed tomography (SPECT) imaging agents and camera hardware have sparked interest in performing dynamic imaging with that modality (Budinger *et al* 1991, Nakajima *et al* 1991, Chiao *et al* 1994); however, dynamic imaging with SPECT is more challenging than it is for PET. The high levels of statistical noise present in dynamic SPECT data greatly limit the confidence with which kinetic parameters can be estimated (Huesman and Mazoyer 1987, Welch *et al* 1995). Likewise, kinetic parameter estimates may exhibit bias arising from factors such as attenuation, detector–collimator response, scatter, inconsistent projections and others

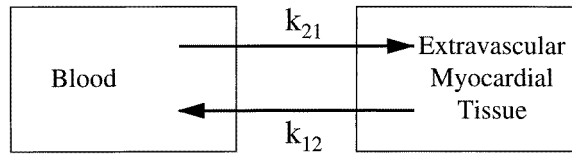


Figure 1. A two-compartment model for the wash-in (k_{21}) and wash-out (k_{12}) of teboroxime between the blood and the extravascular myocardial tissue.

(Links *et al* 1991, Smith and Gullberg 1994, Welch *et al* 1995, Ross *et al* 1997). Many of these factors have parallels in dynamic PET, but the relative importance and extent of degradation for each factor differs. The bias and noise properties of kinetic parameter estimates depend upon how the data are reconstructed and analysed, and they are sensitive to the manner in which compensation for image degrading factors is applied. It is important to understand the underlying properties associated with estimating kinetic parameters from noisy data both with and without compensation for degrading processes. A fundamental understanding of these properties is necessary to guide future research, leading to improved methods for reconstructing and analysing dynamic SPECT data.

There were two main objectives in this work. The first was to formulate a methodology for studying the full solution to the problem of reconstruction and kinetic parameter estimation in dynamic SPECT imaging. The methodology developed here provides a means for analytically calculating the propagation of errors from the acquired data through the reconstruction and parameter estimation steps, and allows for components of error due to bias and statistical fluctuations to be separately studied. The interplay between the data and the analysis models can be evaluated, and the methodology provides a framework for hypothesis testing in a powerful manner. Furthermore the methodology utilizes the full reconstruction solution, by which we mean the completely unregularized exact solution to the reconstruction problem. The full reconstruction solution has received little attention in tomographic imaging literature, and the behaviour of the full solution is not well understood.

The second objective of this work was to use the new methodology to evaluate several fundamental issues regarding dynamic cardiac imaging with ^{99m}Tc -teboroxime (Smith *et al* 1994, 1996, Smith and Gullberg 1994, Chiao *et al* 1994). Teboroxime is a neutral lipophilic compound with high myocardial extraction and rapid wash-out kinetics, making it well-suited for dynamic imaging (Leppo *et al* 1991). Teboroxime kinetics can be modelled using the two-compartment model shown in figure 1. Here the wash-in and wash-out parameters are denoted by k_{21} and k_{12} respectively. The activity concentration $A(t)$ in the myocardium is related to the activity concentration in the blood, $B(t)$, and the kinetic parameters by

$$A(t) = (1 - f_v)k_{21} \int_0^t e^{-k_{12}\tau} B(t - \tau) d\tau + f_v B(t). \quad (1)$$

where f_v represents the vascular fraction in the myocardial region. It has been suggested that wash-in of teboroxime may provide a more sensitive measure of ischaemia than can be obtained from static imaging of perfusion agents (Smith 1994, Gullberg *et al* 1998).

We investigate the relationships between image degrading factors, reconstruction estimators, bias and noise for dynamic teboroxime imaging, with the goal of characterizing the parameter estimation problem so that improved reconstruction and analysis methods can knowledgeably be developed. The effects of image degrading factors and their compensation have not previously been studied for the full reconstruction solution in dynamic SPECT. Furthermore, the trade-off between reduced bias and the noise increase accompanying full

compensation for these effects has not been previously studied. The results of this work can be used to gauge the relative importance of compensating for these effects in the context of dynamic SPECT imaging, for which the management of statistical noise is a paramount concern.

The issue of statistical noise brings up another consideration—regularization methods, which are inherently biased, are commonly used to control noise effects in dynamic imaging, but the use of statistically efficient estimation methods has not been fully evaluated. Here, an estimator is said to be more ‘statistically efficient’ than another estimator if it produces estimates with lower variance at the same degree of bias. It is desirable to control noise by using statistically efficient estimators, which do not increase bias, when quantitative accuracy is required. We have evaluated the extent to which a statistically efficient estimation technique can replace regularization methods in dynamic SPECT imaging. The weighted least-squares (WLS) reconstruction operator was chosen for the statistically efficient approach, and it was compared with the unweighted least-squares reconstruction operator, which is more computationally efficient but less statistically efficient. Other statistically efficient reconstruction operators exist, for example maximum likelihood (which is more statistically efficient than WLS for Poisson distributed data). The WLS operator was chosen for this work because it represents a ‘nearly linear’ reconstruction operator for which the covariance matrix of the reconstructed image can be analytically computed.

The study was performed using a simulation experiment which allowed for the effects of statistical noise and image degrading factors to be studied in a manner that would not be possible using experimentally acquired data. Data analysis was performed using the following methods, which allow for both analytical propagation of errors and analysis of the full reconstruction solution. The data were reconstructed using the singular value decomposition (SVD) based generalized matrix inverse reconstruction algorithm. Weighted and unweighted reconstruction operators were used, and model-based compensation for the image degrading factors was successively applied. The SVD-based algorithm allows for the covariance matrices of the reconstructed images to be calculated analytically. Tissue and blood time–activity curves (TACs) were obtained by drawing regions of interest (ROIs) on the time series of reconstructed images. Given the TAC and corresponding covariance data, the nonlinear fitting package RFIT (Huesman *et al* 1995, Huesman and Mazoyer 1987) was used to calculate the best-fit wash-in and wash-out parameters and their uncertainties. These data describe the expected values and standard deviations of the statistical distributions of the parameters that would be estimated from noisy data, thereby providing a powerful means for analysing the bias and noise properties for the cases studied.

2. Methods

2.1. Simulation experiment

The simulated dynamic SPECT acquisition sequentially acquired 41 time frames of projection data over a 15 min period according to the following sampling schedule: twenty 5 s scans, ten 10 s scans, eight 50 s scans and three 100 s scans. This imaging sequence was found to have sufficient temporal resolution during the fast initial kinetics while keeping the total number of time frames down to a reasonably manageable number. The dynamic phantom and acquisition particulars are given in the following subsections.

2.1.1. Dynamic phantom. A dynamic version of the MCAT phantom (Terry *et al* 1990, Tsui *et al* 1994) was created with different activity distributions corresponding to each time frame

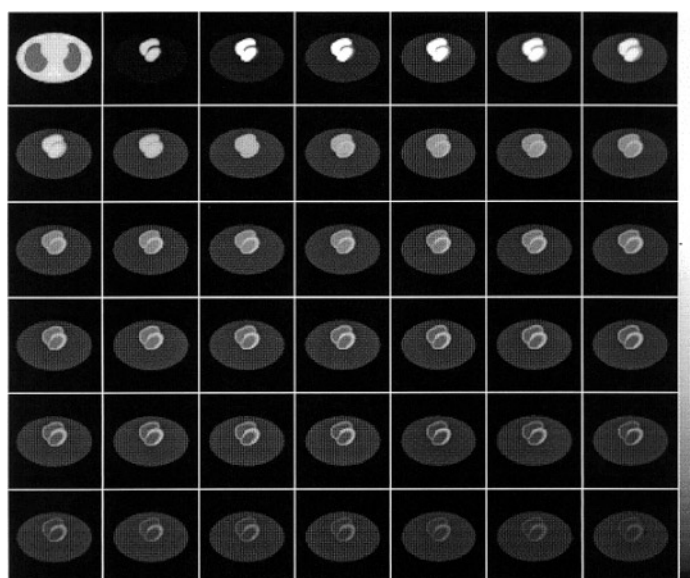


Figure 2. Image of the MCAT phantom attenuation map (top left), followed sequentially by the time series of images for the dynamic activity phantom. The changing activity in the various tissues can be followed as the time series moves from left to right, top to bottom.

of the dynamic acquisition. Due to the memory requirements of the SVD algorithm, only a single 2D slice of the phantom was used for the experiment. The phantom had a 36×24 cm body contour, and it was first created on a 192×192 array using 2.373 mm pixels. It was then collapsed to a 64×64 array of 7.12 mm pixels used for the projection and reconstruction steps of the analysis. Digitization of the phantom onto 7.12 mm pixels was subject to some degree of aliasing, and this digitization was performed prior to generating projections in order to separate aliasing artefacts out from the projection/reconstruction problem. A static version of the phantom was first constructed one organ at a time, including heart, blood pool, lungs and soft tissue background. Since the expected heart cycle duration (≤ 1 s) was much less than the shortest scan length (5 s), no explicit frame-by-frame beating heart model was used; however, blurring due to heart motion was included by using the MCAT beating heart model (Pretorius *et al* 1997) and computing the time-average over the cardiac cycle. The dynamic phantom was constructed by summing each organ of the static phantom using weights (derived from the TACs described below) for each time frame. In this way a series of 2D phantoms was constructed, one for each time frame of the dynamic acquisition. The phantom attenuation map and activity images are shown in figure 2.

The time-activity curves for the blood pool, myocardium and background (soft tissue and lungs) were chosen to mimic those seen in patient studies performed at this institution. Of special interest, the blood TAC was defined by the sum of three decaying exponentials preceded by a 20 s ramp function, and the myocardium TAC was constructed using the blood as input function, with wash-in and wash-out parameters of 0.8 min^{-1} and 0.4 min^{-1} respectively. The vascular fraction in the myocardial tissue (f_v) was set to zero for the purposes of this experiment. The TACs for the blood, myocardium and background are plotted in figure 3. Each TAC was numerically integrated over the active acquisition time for each time frame in order to obtain the weights used to form the dynamic phantom.

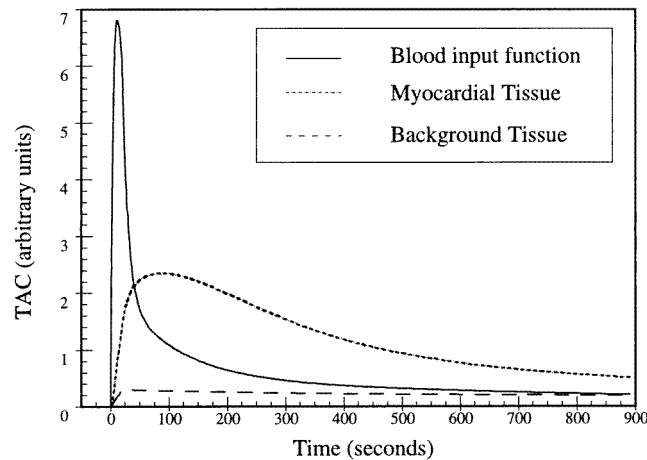


Figure 3. Time-activity curves for the simulation experiment: blood input function, extravascular myocardial tissue and background tissue (lungs and soft tissue background).

2.1.2. Projection data. Projection data for the simulated acquisition were formed by projecting each time frame of the dynamic phantom. The projection models and array sizes were identical to those used later for image reconstruction, ensuring that the simulated projections would be consistent for the reconstruction problem; in practice, aliasing artefacts and modelling errors would likely lead to some degree of bias in the results. The results obtained in this paper will be somewhat positively biased as compared with what can be expected in practice because the aliasing artefacts and modelling errors were eliminated. This approach was advantageous for this paper because, by using consistent models for projection and reconstruction, the effects of image degrading factors could be studied separately from other sources of error.

For each timeframe, all projection angles were assumed to be measured simultaneously. In practice a rotating camera-based system would probably be used for dynamic SPECT; the activity would be actively changing as the gantry is rotated for the acquisition, and data inconsistencies between projection angles would result. Other studies have been performed to assess the effects of using a rotational acquisition geometry for dynamic imaging (Links *et al* 1991, Ross *et al* 1997). In order to separate these effects from those studied in this work, the rotational geometry was not simulated here.

The projection data were simulated using a rotation-based projector (Frey *et al* 1993) which modelled the effects of non-uniform attenuation, depth-dependent collimator-detector response and scatter (Frey and Tsui 1996, Kadrmas *et al* 1998). The projection matrix was calculated using line source geometries in order to provide a pseudo-3D model that accounted for the 3D contributions of detector response and scatter. A low-energy high-resolution (LEHR) parallel hole collimator was used with a circular orbit, and each scan consisted of 120 projection angles evenly spaced over 360° . Data were acquired within a 15% wide energy window centred at 140 keV, and the camera was modelled with an energy resolution of 10% FWHM at 140 keV and 4 mm intrinsic spatial resolution.

Several data sets were simulated, successively including the effects of attenuation, detector response and scatter. The projection data were scaled to 1.8×10^6 total counts over the 15 min acquisition when including attenuation effects. When attenuation effects were not included,

the data were scaled to 6.3×10^6 total counts, and when both attenuation and scatter effects were included the count level was 2.1×10^6 . Poisson noise was simulated at these count levels so that both mean (noise-free) and noisy data sets were obtained. In the following section we demonstrate that the noise-free projection data, which are the expected values, and the known statistical distribution of the projection data are sufficient to analytically calculate the bias and variance of the kinetic parameter estimates. As such, the noisy projection data sets were used only to generate example results for a single noise realization of the data.

2.2. Reconstruction estimators

The data were reconstructed using the generalized matrix inverse (GMI) approach (Huesman *et al* 1977) with SVD methods (Smith *et al* 1992) as briefly described here. The SPECT imaging process can be represented as a linear system of equations

$$\mathbf{F}\bar{\mathbf{x}} = \bar{\mathbf{p}} \quad (2)$$

where \mathbf{F} is the system transfer matrix, $\bar{\mathbf{x}}$ is the mean (noise-free) image vector, and $\bar{\mathbf{p}}$ is the mean (noise-free) projection data vector. The problem of reconstruction is to obtain an estimate of the image ($\hat{\mathbf{x}}$) from a (noisy) measurement of the projection data ($\tilde{\mathbf{p}}$).

The weighted least-squares reconstructed image can be obtained by using SVD to solve the following equation:

$$(\mathbf{F}^T \Phi^{-1} \mathbf{F})\bar{\mathbf{x}} = \mathbf{F}^T \Phi^{-1} \bar{\mathbf{p}} \quad (3)$$

where Φ represents the covariance matrix of the projection data. In SPECT the projection data are Poisson distributed with uncorrelated noise, so Φ is diagonal, and its diagonal elements are given by the means of the corresponding projection data elements (recall the variance equals the mean for the Poisson distribution). Since the expected values of the data are generally not known, an estimate of the covariance matrix $\tilde{\Phi}$ must be used. See the appendix for more details on the estimation of Φ from measured data.

The SVD of $(\mathbf{F}^T \tilde{\Phi}^{-1} \mathbf{F})$ from (3) can be written as $\mathbf{V}\mathbf{S}\mathbf{V}^T$, where \mathbf{V} is the unitary matrix of right singular vectors and \mathbf{S} is the diagonal matrix of singular values. Here we have used the fact that $(\mathbf{F}^T \tilde{\Phi}^{-1} \mathbf{F})$ is symmetric. Given a measurement of the projection data, $\tilde{\mathbf{p}}$, the WLS reconstructed image, $\hat{\mathbf{x}}_{\text{WLS}}$, is given by

$$\hat{\mathbf{x}}_{\text{WLS}} = \mathbf{V}\mathbf{S}^\dagger \mathbf{V}^T \mathbf{F}^T \tilde{\Phi}^{-1} \tilde{\mathbf{p}} \quad (4)$$

where \mathbf{S}^\dagger represents the pseudo-inverse of \mathbf{S} .

The unweighted least-squares (LS) reconstruction is obtained by replacing the projection data covariance matrix, Φ , by the identity matrix in (3), thereby assigning a uniform weight to all projection data. The SVD is performed upon $\mathbf{F}^T \mathbf{F}$, yielding $\mathbf{V}_{\text{LS}} \mathbf{S}_{\text{LS}} \mathbf{V}_{\text{LS}}^T$, and the unweighted LS reconstruction is obtained:

$$\hat{\mathbf{x}}_{\text{LS}} = \mathbf{V}_{\text{LS}} \mathbf{S}_{\text{LS}}^\dagger \mathbf{V}_{\text{LS}}^T \mathbf{F}^T \tilde{\mathbf{p}}. \quad (5)$$

The expected values of the reconstructed images directly reflect the bias, if any, in the images. Equation (5) represents a linear reconstruction operator, and the expected value of the unweighted LS reconstructed image is easily obtained by reconstructing the expected values, i.e. noise-free, projection data. This calculation is a bit more subtle for the WLS case in which the reconstruction operator implicitly depends upon $\tilde{\Phi}$, which is estimated from $\tilde{\mathbf{p}}$. The WLS reconstruction operator is actually nonlinear in this case; however, the accuracy of estimating $\tilde{\Phi}$ improves with counting statistics. A very good estimate of the expected value of the WLS reconstruction can be obtained by reconstructing noise-free projection data, which is analogous to the limiting case of acquiring very high statistics.

The reconstruction of a large number of images using the generalized matrix inversion approach is both memory and computationally intensive. In order to reduce these demands, we limited the image space to contain only those pixels inside, or within two pixels (14 mm) of, the phantom body contour as defined by the attenuation map. This reduced the dimension of the image space from 4096 to 1748, leading to substantially reduced computational requirements. The SVDs and image reconstructions were performed on a Cray T916 (North Carolina Supercomputer Center, Durham, NC), and approximately 2 CPU hours were required for WLS reconstruction of each series of 41 timeframes. As a guide for the interested reader, we timed a single WLS reconstruction on 1 CPU of a 300 MHz Sun Enterprise 3000. Based on those data, we estimate that about 7 days 16 h would have been required on the Sun workstation for WLS reconstruction of a series of 41 timeframes.

2.3. Calculation of reconstructed image covariance matrices

Given the covariance matrix of the measured data, the SVD-based GMI reconstruction approach allows for direct analytical calculation of the covariance matrices of the reconstructed images. Alternatively, the covariance matrices could have been estimated empirically by reconstructing a large number of noise realizations of the data and analysing the resulting ensemble of images. However, such an approach would have required much more computational effort than the deterministic approach used here in order to gain the statistical power necessary to significantly differentiate between the cases studied. We use the expected values and known statistical behaviour of the projection data to directly calculate the covariance matrices of the reconstructed images.

The details regarding calculation of the reconstructed image covariance matrices are given in the appendix, along with a discussion of the validity domain as applied to SPECT reconstruction. For the statistically weighted case, the covariance matrix of the WLS reconstructed image is given by

$$\text{COV}(\hat{x}_{\text{WLS}}) = \mathbf{V}\mathbf{S}^\dagger\mathbf{V}^T. \quad (6)$$

The covariance matrix for the unweighted LS reconstruction is obtained in a similar manner, though less simplification occurs within the derivation. The resultant working expression is written as

$$\text{COV}(\hat{x}_{\text{LS}}) = \mathbf{V}_{\text{LS}}\mathbf{S}_{\text{LS}}^\dagger\mathbf{V}_{\text{LS}}^T\mathbf{F}^T\Phi\mathbf{F}\mathbf{V}_{\text{LS}}\mathbf{S}_{\text{LS}}^\dagger\mathbf{V}_{\text{LS}}^T. \quad (7)$$

2.4. Estimation of kinetic parameters

Two sets of ROIs were drawn on the reconstructed images as shown in figure 4 in order to obtain the blood input function and myocardium TAC. The first set of ROIs consisted of 7 pixels inside the left ventricle (LV) chamber and 5 pixels on the LV wall. These ROIs were carefully chosen to include only pixels entirely situated within the blood pool or myocardium of the phantom, and the resulting TACs are used for local kinetic parameter estimates that are not biased due to discretization errors. The second set of ROIs were chosen to be the same size as those that would be used for regional kinetic parameter estimation in practice. Such regional parameters would typically be measured using ROIs that span many slices and contain approximately 20–25 voxels of myocardium. Since the computational and memory demands of the SVD algorithm limited our analysis to only a single slice, we created large ROIs that contained 22 pixels in the blood pool and 26 pixels of the myocardial wall. These ROIs essentially contain the entire LV wall and blood pool for this slice. The TACs for the large ROIs will have noise levels on the same order as would be seen clinically for regional parameter estimation, but

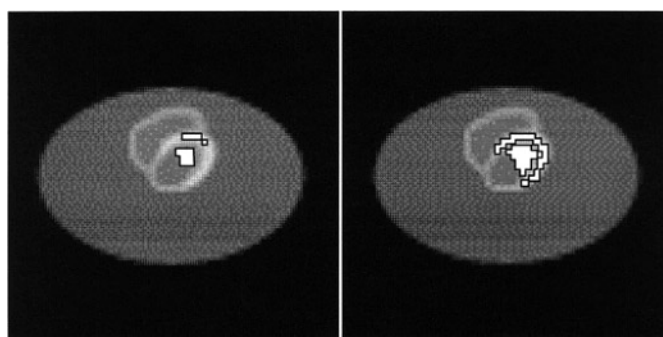


Figure 4. The locations of the blood and myocardial ROIs as drawn on the MCAT phantom: left, small ROIs used to estimate local kinetic parameters; right, large ROIs used to imitate estimating regional kinetic parameters from a 3D image.

they also introduce a degree of bias due to partial volume discretization errors (some pixels in the large ROIs contain partial components due to blood, heart tissue or background tissue). The TACs for each ROI were obtained by averaging the pixel values in each ROI for each time frame. Likewise, the covariance matrices of the reconstructed images were used to calculate the variance of each ROI and the correlations between ROIs. The kinetic parameters wash-in (k_{21}), wash-out (k_{12}) and vascular fraction (f_v) were estimated by fitting the TACs and tomographically acquired blood input functions to the two-compartment model using RFIT, which also calculates the variance and correlations of these parameters using the data provided (Huesman and Mazoyer 1987, Huesman *et al* 1995).

3. Results

Figure 5 shows sample timeframes of the noise-free and noisy WLS reconstructed images for the case in which attenuation effects were simulated in the data and compensated for in the reconstruction. The effects of scatter and the detector–collimator response function were neither included in the simulation nor compensated for in this case. Note that the noise-free images represent the expectation values of the reconstructed pixel values, and that the noisy images provide an example of what is obtained for a single noise realization of the data. The local (small ROI) and regional (large ROI) kinetic parameters for these data are shown in figure 6, where the indicated standard deviations were calculated using the analytical methods described earlier (the results for noisy data provide only an estimate of the parameters and uncertainties for that noise realization, whereas the noise-free results give the expectation values and analytically calculated standard deviations for these random variables). Since the analytical formulation fully describes the bias and variance of the parameter estimates, no further results from noisy realizations of the data are presented.

The data presented in figure 6 also reveal an important detail. The data exhibit strikingly high levels of statistical noise, especially for the local parameter estimates. The large ROI results imitate regional parameter estimation for 3D imaging, yet these estimates still contain considerable uncertainty due to statistical noise (standard deviations of the order of 10% of the mean). While the noise levels are much lower than seen for the local parameter estimation problem, they are still high enough to be a primary issue of concern for dynamic SPECT imaging. Recall, however, that the full reconstruction solution was obtained and that no regularization was performed. In practice the user would need to evaluate the degree

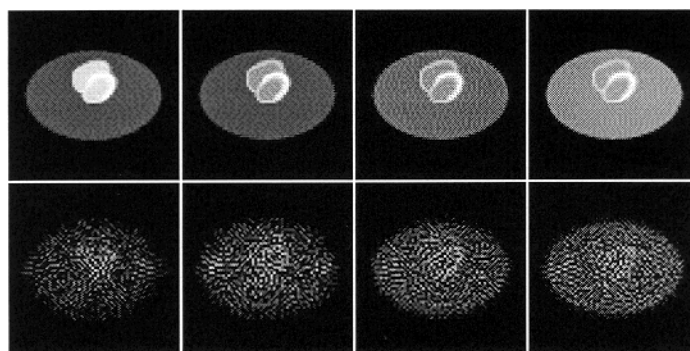


Figure 5. Sample noise-free (top row) and noisy (bottom row) reconstructed images for the case which included attenuation compensation but no other effects. Timeframes shown are at 1 min (far left), 3 min (left middle), 8 min (right middle) and 15 min (far right) after injection.

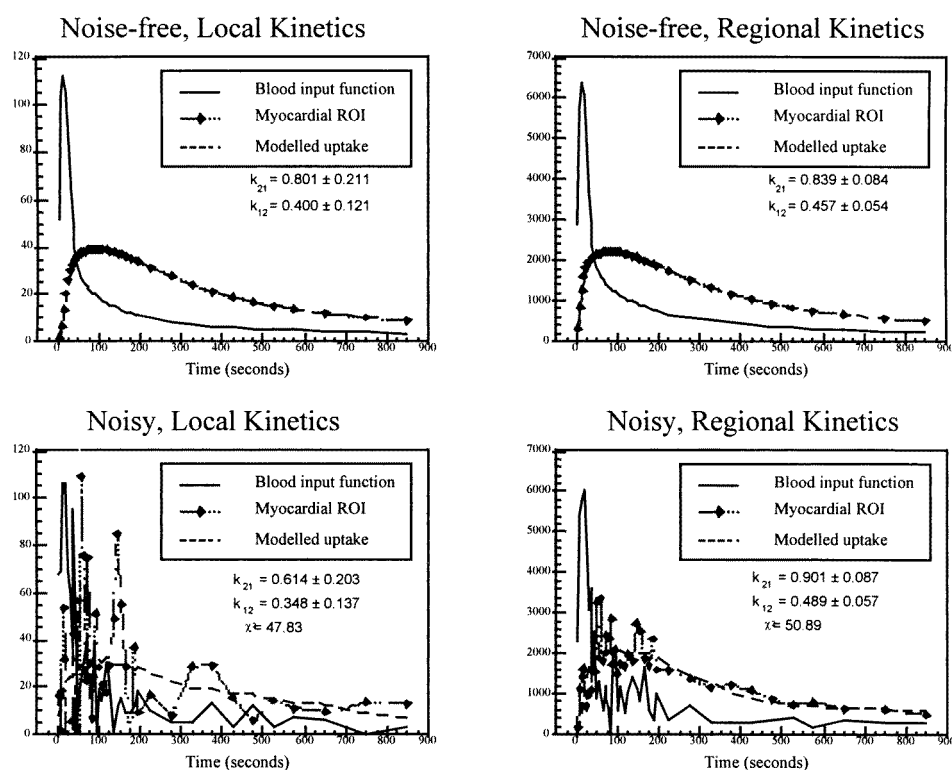


Figure 6. Reconstructed TACs (arbitrary units) and modelled uptake curves for the case which included attenuation compensation and no other effects: expected values (top row), one realization of noisy data (bottom row). The TACs in the left column were created using the small ROIs, and the TACs in the right column used the large ROIs. The estimated kinetic parameters are shown, with chi-squared values for the noisy fits (38 degrees of freedom).

of statistical uncertainty acceptable for the application of interest, then regularize the data, accepting some increase in bias in exchange for controlling statistical variations. The value of

Table 1. Local kinetic parameter estimates (expectation value of fit \pm standard deviation) for each case studied. The fitted value of the vascular fraction in the myocardial ROI (f_v) is also given, as well as the chi-squared values for the (noise-free) fits.

Effects included in data [†]	Effects compensated for [†]	WLS		LS	
		k_{21} (min ⁻¹) f_v	k_{12} (min ⁻¹) chi-squared	k_{21} (min ⁻¹) f_v	k_{12} (min ⁻¹) chi-squared
	True values	0.800 0.000	0.400 n/a	0.800 0.000	0.400 n/a
None	None	0.801 \pm 0.325 -0.001 \pm 0.315	0.400 \pm 0.188 1.74×10^{-4}	0.801 \pm 0.370 -0.001 \pm 0.409	0.400 \pm 0.212 1.02×10^{-4}
A	None	3.44 \pm 8.07 0.294 \pm 2.09	0.578 \pm 1.31 5.14×10^{-2}	0.993 \pm 1.642 0.297 \pm 1.173	0.353 \pm 0.657 5.93×10^{-3}
A	None	1.06 \pm 0.363	0.503 \pm 0.175		
	(Regularized)	-0.112 \pm 0.314	1.90×10^{-1}		
A	A	0.801 \pm 0.211 -0.001 \pm 0.200	0.400 \pm 0.121 4.26×10^{-4}	0.801 \pm 0.215 -0.001 \pm 0.214	0.400 \pm 0.123 3.64×10^{-4}
AD	A	0.749 \pm 0.260 0.184 \pm 0.208	0.411 \pm 0.160 1.17×10^{-3}	0.751 \pm 0.264 0.188 \pm 0.220	0.410 \pm 0.161 8.51×10^{-3}
AD	AD	0.801 \pm 0.664 -0.001 \pm 0.610	0.400 \pm 0.377 4.56×10^{-5}	0.801 \pm 0.674 -0.001 \pm 0.651	0.400 \pm 0.382 3.94×10^{-5}
ADS	A	0.756 \pm 0.273 0.256 \pm 0.201	0.444 \pm 0.178 1.61×10^{-3}	0.757 \pm 0.276 0.254 \pm 0.210	0.445 \pm 0.179 1.33×10^{-3}
ADS	ADS	0.801 \pm 0.710 -0.001 \pm 0.674	0.400 \pm 0.401 3.72×10^{-5}	0.801 \pm 0.721 -0.001 \pm 0.713	0.400 \pm 0.407 3.30×10^{-5}
ADS	ADS	0.773 \pm 0.190	0.410 \pm 0.103		
	(Regularized)	0.099 \pm 0.148	5.11×10^{-2}		

[†] A = attenuation, D = detector response, S = scatter.

the results presented in this work is that they quantify the degree to which such regularization is necessary; this is especially important when considering the use of statistically efficient estimators (section 3.1) or when compensating for image degrading factors (sections 3.2 and 3.3).

3.1. Statistically efficient estimation

One aim of the study was to evaluate the extent to which statistically efficient estimation methods can replace regularization methods to control the effects of statistical noise. The answer to this question lies in comparing the standard deviations of the WLS and LS parameters for local or regional estimates as presented in tables 1 and 2 respectively. Significant high-performance computing resources (approximately 30 CPU hours on a Cray T916) were required to generate these data. In accordance with theoretical predictions, the WLS reconstruction approach consistently led to parameter estimates with lower statistical deviations than did the unweighted LS reconstructions. The only exception was the case in which attenuation was present but not compensated for, which led to extreme model mismatch, very high bias and meaningless parameter estimates.

These results verify that the WLS reconstruction operator is more statistically efficient than the unweighted LS operator. However, the reduction in standard deviation for the WLS operator was small in all cases studied, and negligible in most cases. This was somewhat surprising, and indicates that accurate statistical modelling may not be highly beneficial for dynamic SPECT imaging. In many cases the increased computation burden required to use

Table 2. Regional kinetic parameter estimates (expectation value of fit \pm standard deviation) for selected cases. The fitted value of the vascular fraction in the myocardial ROI (f_v) is also given, as well as the chi-squared values for the (noise-free) fits.

Effects included in data [†]	Effects compensated for [†]	WLS		LS	
		k_{21} (min ⁻¹) f_v	k_{12} (min ⁻¹) chi-squared	k_{21} (min ⁻¹) f_v	k_{12} (min ⁻¹) chi-squared
None	None	0.839 \pm 0.236 0.083 \pm 0.167	0.457 \pm 0.153 7.49×10^{-4}	0.838 \pm 0.272 0.083 \pm 0.226	0.457 \pm 0.175 4.24×10^{-4}
A	A	0.839 \pm 0.084 0.083 \pm 0.055	0.457 \pm 0.054 6.79×10^{-3}	0.839 \pm 0.086 0.083 \pm 0.058	0.457 \pm 0.054 6.01×10^{-3}
AD	A	0.816 \pm 0.109 0.234 \pm 0.061	0.510 \pm 0.076 2.09×10^{-2}	0.818 \pm 0.110 0.235 \pm 0.064	0.509 \pm 0.077 1.68×10^{-2}
AD	AD	0.839 \pm 0.222 0.083 \pm 0.159	0.457 \pm 0.142 8.12×10^{-4}	0.839 \pm 0.226 0.083 \pm 0.167	0.457 \pm 0.144 7.41×10^{-4}
ADS	A	0.812 \pm 0.113 0.301 \pm 0.059	0.538 \pm 0.082 2.82×10^{-2}	0.815 \pm 0.115 0.300 \pm 0.062	0.540 \pm 0.083 2.42×10^{-2}
ADS	ADS	0.839 \pm 0.239 0.083 \pm 0.176	0.457 \pm 0.152 6.78×10^{-4}	0.839 \pm 0.243 0.083 \pm 0.183	0.457 \pm 0.154 6.28×10^{-4}
ADS	ADS (Regularized)	0.825 \pm 0.084 0.137 \pm 0.050	0.455 \pm 0.048 6.71×10^{-2}		

[†] A = attenuation, D = detector response, S = scatter.

statistically efficient estimation techniques may not be justified considering the marginal gain. One could speculate that using a single, ‘average’ set of weights for the entire time series of reconstructions would be a relatively efficient approach, both in terms of computational effort and statistical uncertainty.

3.2. Image degrading factors

The data in tables 1 and 2 illustrate the effects that attenuation, detector response and scatter have upon kinetic parameter estimates. Selected results are presented graphically in figure 7, which plots the TACs and modelled uptake curves for a number of cases both with and without compensation. These data characterize the effects of model mismatch upon the bias and noise levels in kinetic parameter estimates; when considered in conjunction with the results of the next section regarding full compensation, the data characterize the limits of the bias–noise trade-off associated with these effects.

In the absence of image degrading factors, the local kinetic parameter estimates were nearly identical to the true values, indicating that the simulations were accurately performed. The vascular fraction in the myocardium ROI (f_v) was also estimated accurately. On the other hand, the regional kinetic parameter estimates were considerably biased. Recall that the small ROIs used for the local parameters were carefully chosen to include only pixels entirely situated within the blood or myocardium of the phantom, whereas the large ROIs used for the regional parameters had some pixels partially containing multiple components of the phantom. This resulted in ‘spillover’ between the blood, myocardial and background data, thereby compromising the TACs and biasing the data. Because of this bias in the regional parameter estimates, the local parameter estimates are best used to study the effects of image degrading factors and their compensation.

Each image degrading factor introduced some degree of bias into the kinetic parameter estimates as expected. We leave it up to the reader to assess the relative impact of each image

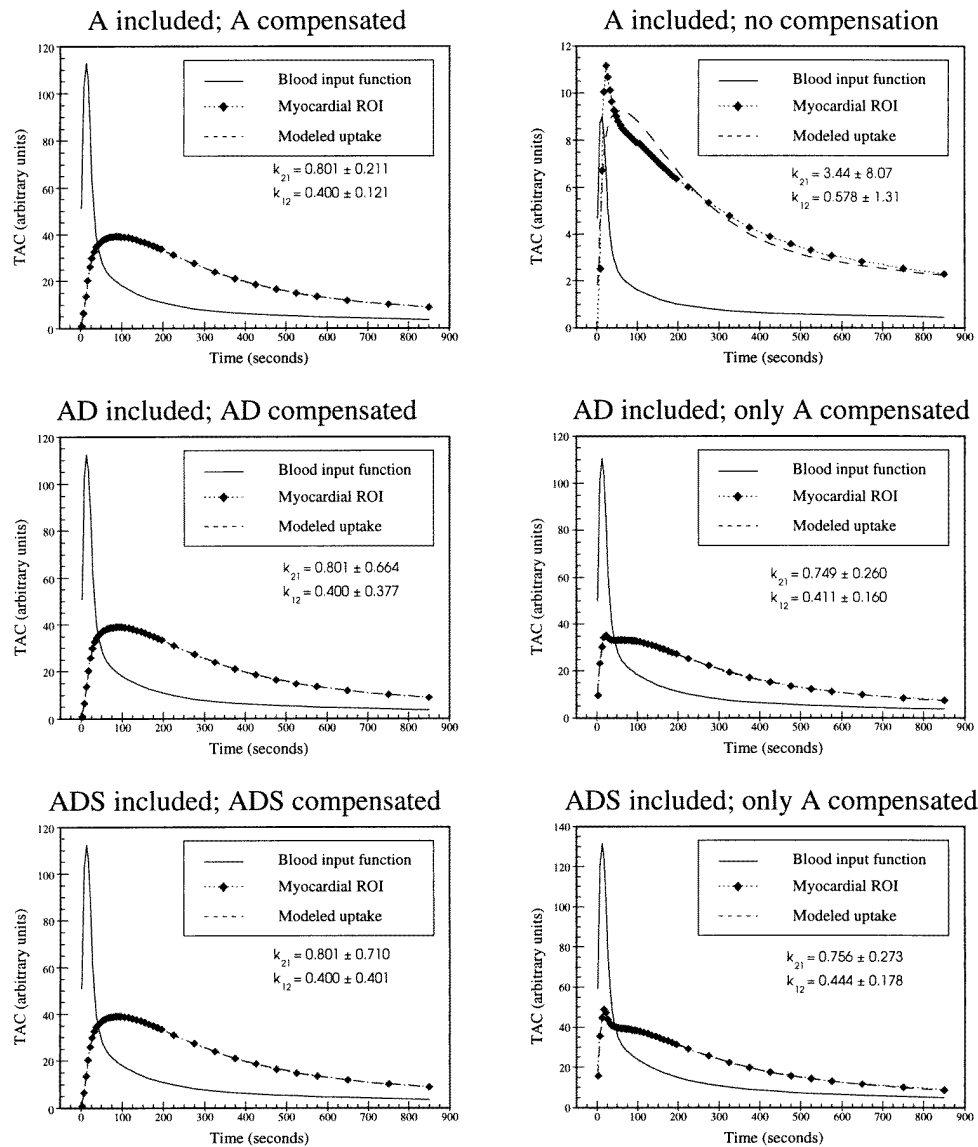


Figure 7. TAC expectation values and modelled uptake curves demonstrating the effects of attenuation, detector response and scatter, and compensation for these effects. Local kinetics using the small ROIs are shown. The effects included in the data and those compensated for are listed above each plot (A = attenuation, D = detector response, S = scatter).

degrading factor at the full reconstruction solution as compared to his/her preconceived notions, though the excessive bias associated with attenuation effects deserves additional comment. The strikingly high levels of bias caused by the uncompensated presence of attenuation effects were somewhat surprising, and were higher than typically seen in conventional reconstructions which do not approach the full solution. This can be attributed to the fact that, at the full reconstruction solution, all components of the reconstructed image are forced to match the

projection data as closely as possible. It is interesting to note that much of the structure of the attenuation artefacts was associated with the latter singular vectors of the SVD-GMI reconstruction. The latter singular vectors correspond to the small singular values, indicating that these components of the image are harder to recover from the measured projections. In order to demonstrate this point, we regularized the attenuated reconstruction by zeroing all singular values less than 0.1% of the largest singular value. As seen in table 1, the resultant data retained considerable bias, but this bias was much reduced as compared to the unregularized attenuated case.

3.3. Compensation for image degrading factors

The data in tables 1 and 2 can also be used to assess the bias–variance trade-off associated with ideal, unregularized compensation for each image degrading factor. Note that full compensation for all image degrading factors is required in order to minimize bias, but undesired noise increases may accompany such compensation. Compensation for detector response and scatter effects was found to markedly increase the statistical uncertainty in the parameter estimates. The data for uncompensated versus compensated cases bracket the bias and noise levels for each factor. It will be useful to consider these results in the future development of compensation methods for dynamic SPECT, since the performance of regularized/partial compensation for image degrading factors can be expected to fall within the limits calculated here. For example, consider the case of detector response blurring versus compensation (items 6 and 7 of table 1). Detector response blurring caused biases of -6.4% and $+2.8\%$ in k_{21} and k_{12} respectively. Full compensation for detector response blurring effectively removed these biases, but increased the statistical uncertainties from 35–39% of the mean to 83–94% of the mean. Clearly, in this case the increased sensitivity to statistical noise associated with *unregularized* detector response compensation outweighed the benefits of performing such compensation. Therefore, the successful application of a regularized method of performing detector response compensation that has a beneficial bias–variance trade-off is essential.

To demonstrate the potential benefits of performing regularization, we repeated the analysis for the case with attenuation, detector response and scatter effects, but regularized the WLS reconstruction by zeroing all singular values less than 0.1% of the largest singular value. That is, the singular value spectra were truncated so that the image components most sensitive to noise in the data were excluded from the reconstruction. We emphasize that this simplistic regularization scheme was not optimized, but it was sufficient for demonstration purposes. The results are shown in the final row of table 1. The compensated and regularized images resulted in kinetic parameters with less bias (-3.4%) than in the uncompensated case (-5.5%), and the variances were much lower than in the corresponding unregularized cases (25% of mean versus 89%). As a result, the regularized parameter estimates for noisy data could be believed with substantially more confidence. This example demonstrates the bias–variance trade-off associated with regularization, as well as the potential benefits associated with regularization. It will be important to consider these aspects when designing regularization schemes to be used in practice.

4. Discussion and conclusions

In this paper we have formulated a methodology for analytically studying the bias and noise properties of the full solution to the reconstruction/parameter estimation problem in dynamic SPECT imaging. Using this analysis tool, we have studied relationships between

reconstruction estimators, image degrading factors, bias and statistical noise in dynamic cardiac SPECT imaging with teboroxime. One goal was to evaluate the extent to which statistically efficient estimation techniques could replace biased regularization methods for noise control. Unexpectedly, it was found that the WLS reconstruction operator provided only minor reductions in noise levels as compared to the unweighted LS operator. This result was only evaluated for the specific case studied, though we speculate that a similar result might be obtained for other data at similar count levels. We conclude that, for some imaging applications, the increased computational needs of statistically efficient reconstruction operators may outweigh the benefits of using these operators. This point should be considered in the future development of reconstruction methods for dynamic imaging.

A basic investigation into the effects of image degrading factors at the full reconstruction solution was also performed, and ideal compensation for these factors was studied. The bias that each image degrading factor introduced into the full reconstruction solution was calculated in terms of the resultant bias imposed on the kinetic parameter estimates. Ideal compensation for each degrading factor resulted in very low bias results, and the noise increase associated with complete compensation for each factor was calculated. The resultant data delineate the limiting ranges on the bias–noise trade-off concerning compensation for each effect. These data are intended to guide future development of regularization and compensation methods for dynamic SPECT by highlighting the degree of noise control required to achieve beneficial compensation. Additionally, an example of a crude regularization approach was provided to illustrate the potential benefits of regularization.

The results of this study suggest that careful consideration of the choices of reconstruction algorithm, compensation methods and regularization scheme is warranted in order to obtain accurate and precise estimates of the kinetic parameters in dynamic SPECT imaging. The fundamental understanding of the relationships between bias and variance studied in this work fulfils a crucial step in the future development of optimal reconstruction and compensation algorithms for dynamic SPECT data.

Acknowledgments

This work was supported by NIH grant R01 HL50663, and by the Director, Office of Energy Research, Office of Biological and Environmental Research, Medical Applications and Biophysical Research Division of the US Department of Energy under contract No DE-AC03-76SF00098. Computing facilities were available through an academic research grant from the North Carolina Supercomputer Center. The authors would like to thank Dr Eric Frey for his helpful assistance and Dr Benjamin Tsui for his generosity in supplying the MCAT phantom used in this work.

Appendix

A.1. Estimation of the projection data covariance matrix

The projection data covariance matrix, Φ , is generally not known exactly, and it must be estimated from the measured projections, \tilde{p} . We model \tilde{p} to have uncorrelated noise and obey to Poisson statistics. When Φ is diagonal, the diagonal elements are the variances of the corresponding projection data, and the variances equal the means; i.e. $\Phi_{ij} = \tilde{p}_i \delta_{ij}$. One way to estimate the projection data covariance matrix would be to use $\tilde{\Phi}_{ij} = \tilde{p}_i \delta_{ij}$, where the tilde denotes that this is an estimate of Φ . For our application this may not be the best approach. In order to compute the WLS reconstructed image Φ must be inverted, but the above expression

gives $\tilde{\Phi}$ singular if any of the \tilde{p}_i are zero. In addition, this $\tilde{\Phi}$ estimate may result in a biased image: suppose that, for a given element j , a noisy measurement yielded $\tilde{p}_j = 0$ but the expected value was $\bar{p}_j = 0.5$. An erroneously high weight would be given to \tilde{p}_j and a biased solution would result.

The above problems can be greatly reduced if a lower threshold is defined for Φ such that

$$\tilde{\Phi}_{ij} = \begin{cases} \tilde{p}_i \delta_{ij} & \tilde{p}_i \geq \lambda \\ \lambda \delta_{ij} & \text{otherwise.} \end{cases} \quad (8)$$

In our experience, a threshold value of $\lambda = 1.0$ gives good results when estimating $\tilde{\Phi}$ from noisy projection data. We have not, however, performed a detailed investigation into the optimal choice of λ . In this paper a significant portion of the analysis was performed using the expected values of the projection data. In that case the true covariance matrix is known, and we only need to ensure that $\tilde{\Phi}$ is not singular by choosing λ sufficiently large to avoid numerical errors. We heuristically chose a threshold of $\lambda = 0.01$ for this portion of the analysis.

A.2. WLS reconstruction using SVD

Given that the noise in the projection data is uncorrelated, a statistically weighted version of the imaging equation can be formed by multiplying equation (2) on the left by the weighting matrix, Ψ :

$$\Psi \mathbf{F} \tilde{\mathbf{x}} = \Psi \tilde{\mathbf{p}}. \quad (9)$$

To obtain the weighted least squares, i.e. minimum chi-squared, solution, the statistical weights are given by $1/\sigma_j$, where σ_j is the standard deviation of projection data element \tilde{p}_j . Hence Ψ is diagonal, and $\Psi_{jj} = 1/\sigma_j$.

Equation (9) can be solved using SVD to obtain the SVD solution; however, for practical reasons, we generally first multiply on the left by $\mathbf{F}^T \Psi^T$ to obtain

$$(\mathbf{F}^T \Psi^T \Psi \mathbf{F}) \tilde{\mathbf{x}} = \mathbf{F}^T \Psi^T \Psi \tilde{\mathbf{p}}. \quad (10)$$

Recognizing that $\Psi^T \Psi = \Phi^{-1}$ for Poisson distributed data, equation (10) simplifies to equation (3) of the text. Additional details on these methods can be obtained from Gullberg and Zeng (1994), Kadrmas *et al* (1997) and others.

A.3. Calculation of the covariance matrix of the reconstructed images

When using SVD to obtain the WLS solution to a linear system of equations, it is well known that the covariance matrix of the solution can be readily calculated as well (Press *et al* 1988). In SPECT imaging, however, the statistical weights are not known *a priori* and are estimated from the measured projection data. As a result, the WLS reconstruction problem is nonlinear, and calculation of the covariance matrix of the reconstructed image is more difficult. In this section we derive an approximate expression for the covariance matrix of the WLS image, identifying each of the approximations used.

The covariance matrix of the reconstructed image, $\hat{\mathbf{x}}$, can be calculated using (Kendall *et al* 1987):

$$\text{COV}(\hat{\mathbf{x}})_{ij} = \sum_{k,l=1}^M \frac{\partial \hat{x}_i}{\partial \tilde{p}_k} \Phi_{kl} \frac{\partial \hat{x}_j}{\partial \tilde{p}_l} \quad (11)$$

where M is the length of the projection data vector, $\tilde{\mathbf{p}}$. Equation (11) is exact for $\hat{\mathbf{x}}$ a linear function of $\tilde{\mathbf{p}}$, and is a Taylor approximation otherwise. Also note that $\tilde{\Phi}$ is not known *a priori*

in practice, though it was known exactly for the simulations used in this paper. Equation (4) from section 2.2 gives the expression for the weighted least squares reconstructed image; for the following derivation we will write the matrix inversion explicitly $[(\mathbf{F}^T \tilde{\Phi}^{-1} \mathbf{F})^\dagger = \mathbf{V} \mathbf{S}^\dagger \mathbf{V}^T]$. Given the relationship between $\tilde{\Phi}$ and $\tilde{\mathbf{p}}$, we can simplify $(\tilde{\Phi}^{-1} \tilde{\mathbf{p}})_i = 1$ and write

$$\hat{\mathbf{x}}_{\text{WLS}} = (\mathbf{F}^T \tilde{\Phi}^{-1} \mathbf{F})^\dagger \mathbf{F}^T \tilde{\Phi}^{-1} \tilde{\mathbf{p}} \approx (\mathbf{F}^T \tilde{\Phi}^{-1} \mathbf{F})^\dagger \mathbf{F}^T \mathbf{1} \quad (12)$$

where $\mathbf{1}$ denotes a column vector of all ones. To compute $\text{COV}(\hat{\mathbf{x}}_{\text{WLS}})$ using (11), we need the derivative

$$\begin{aligned} \frac{\partial(\hat{\mathbf{x}}_{\text{WLS}})_i}{\partial \tilde{p}_k} &= - \left[(\mathbf{F}^T \tilde{\Phi}^{-1} \mathbf{F})^\dagger \mathbf{F}^T \frac{\partial \tilde{\Phi}^{-1}}{\partial \tilde{p}_k} \mathbf{F} (\mathbf{F}^T \tilde{\Phi}^{-1} \mathbf{F})^\dagger \mathbf{F}^T \mathbf{1} \right]_i \\ &= - \left[(\mathbf{F}^T \tilde{\Phi}^{-1} \mathbf{F})^\dagger \mathbf{F}^T \frac{\partial \tilde{\Phi}^{-1}}{\partial \tilde{p}_k} (\mathbf{F} \hat{\mathbf{x}}_{\text{WLS}}) \right] \\ &= [(\mathbf{F}^T \tilde{\Phi}^{-1} \mathbf{F})^\dagger \mathbf{F}^T]_{ik} \frac{(\mathbf{F} \hat{\mathbf{x}}_{\text{WLS}})_k}{\tilde{p}_k^2}. \end{aligned} \quad (13)$$

Here we have used the property that $\partial(\mathbf{A}^{-1})/\partial x = -\mathbf{A}^{-1}(\partial \mathbf{A}/\partial x)\mathbf{A}^{-1}$ (Deutsch 1965), which also holds for the pseudo-inverse provided that it is full-rank in the pixel direction. When not full-rank, this property remains valid throughout the range of \mathbf{A} , again sufficient for this derivation. Using (11) and (13), the covariance matrix of the WLS reconstructed image is given by

$$\text{COV}(\hat{\mathbf{x}}_{\text{WLS}}) = (\mathbf{F}^T \tilde{\Phi}^{-1} \mathbf{F})^\dagger \mathbf{F}^T \Psi^{-1} \mathbf{F} (\mathbf{F}^T \tilde{\Phi}^{-1} \mathbf{F})^\dagger \quad (14)$$

where

$$\Psi_{ij} \equiv \frac{\tilde{p}_i^4}{\tilde{p}_i (\mathbf{F} \hat{\mathbf{x}}_{\text{WLS}})_i^2} \delta_{ij} \approx \frac{\tilde{p}_i^3}{(\mathbf{F} \hat{\mathbf{x}}_{\text{WLS}})_i^2} \delta_{ij} \approx \tilde{p}_i \delta_{ij} = \tilde{\Phi}_{ij}. \quad (15)$$

Equations (14) and (15) lead to the working expression for the covariance matrix

$$\text{COV}(\hat{\mathbf{x}}_{\text{WLS}}) \approx (\mathbf{F}^T \tilde{\Phi}^{-1} \mathbf{F})^\dagger = \mathbf{V} \mathbf{S}^\dagger \mathbf{V}^T. \quad (16)$$

This expression is identical to that which would be obtained for the linear WLS solution where the weights do not depend upon the measured data; however, in the nonlinear case equation (16) is an approximation and does not hold in all situations.

The first approximation in (15) is that $\tilde{\mathbf{p}} \approx \bar{\mathbf{p}}$, which improves with better counting statistics. The second approximation in (15) is that $\mathbf{F} \hat{\mathbf{x}}_{\text{WLS}} \approx \tilde{\mathbf{p}}$. This approximation is exact when the data are consistent. If this is not the case, then the WLS reconstruction criterion ensures that $\hat{\mathbf{x}}_{\text{WLS}}$ minimizes the weighted sum of squares of the difference between $\mathbf{F} \hat{\mathbf{x}}_{\text{WLS}}$ and $\tilde{\mathbf{p}}$. That is, the WLS reconstruction criterion ensures that the second approximation in (15) is the best that it can be given the measured data $\tilde{\mathbf{p}}$ and the system model \mathbf{F} . Note that many of the data presented in this paper were based upon simulated data in which the expected values of the data and the actual statistical weights were known *a priori*. Using these data, it was possible to analytically calculate the covariance matrices of the WLS SPECT images to good accuracy.

The covariance matrix of the unweighted least-squares reconstructed image can also be calculated using (11). Recalling the equation (5) for $\hat{\mathbf{x}}_{\text{LS}}$, we compute the derivative

$$\frac{\partial(\hat{\mathbf{x}}_{\text{LS}})_i}{\partial \tilde{p}_k} = [\mathbf{V}_{\text{LS}} \mathbf{S}_{\text{LS}}^\dagger \mathbf{V}_{\text{LS}}^T \mathbf{F}^T]_{ik}. \quad (17)$$

Combining (17) with (11) leads directly to the expression for the covariance matrix

$$\text{COV}(\hat{\mathbf{x}}_{\text{LS}}) = \mathbf{V}_{\text{LS}} \mathbf{S}_{\text{LS}}^\dagger \mathbf{V}_{\text{LS}}^T \mathbf{F}^T \Phi \mathbf{F} \mathbf{V}_{\text{LS}} \mathbf{S}_{\text{LS}}^\dagger \mathbf{V}_{\text{LS}}^T. \quad (18)$$

Note that, for the unweighted case, the least-squares reconstruction problem is linear and equation (18) is exact.

References

- Budinger T F, Araujo L, Ranger N, Coxson P, Klein G, Huesman R and Alavi A 1991 Dynamic SPECT feasibility studies (abstract) *J. Nucl. Med.* **32** 955P
- Chiao P-C, Ficaro E P, Dayanikli F, Rogers W L and Schwaiger M 1994 Compartmental analysis of technetium-99m-teboroxime kinetics employing fast dynamic SPECT at rest and stress *J. Nucl. Med.* **35** 1265–73
- Deutsch R 1965 *Estimation Theory* (Englewood Cliffs, NJ: Prentice-Hall)
- Frey E C, Ju Z W and Tsui B M W 1993 A fast projector-backprojector pair modelling the asymmetric, spatially varying scatter response function for scatter compensation in SPECT imaging *IEEE Trans. Nucl. Sci.* **40** 1192–7
- Frey E C and Tsui B M W 1996 A new method for modelling the spatially-variant, object-dependent scatter response function in SPECT 1996 *IEEE Nuclear Science Symp. and Medical Imaging Conf. (Anaheim, CA)* pp 1082–6
- Gullberg G T, Huesman R H, Ross S G, Di Bella E V R, Zeng G L, Reutter B W, Christian P E and Foresti S A 1998 Dynamic cardiac single photon emission computed tomography *Nuclear Cardiology: State of the Art and Future Directions* ed B L Zaret and G A Beller (New York: Mosby-Year Book) pp 137–87
- Gullberg G T and Zeng G L 1994 A reconstruction algorithm using singular value decomposition of a discrete representation of the exponential radon transform using natural pixels *IEEE Trans. Nucl. Sci.* **41** 2812–19
- Huesman R H, Gullberg G T, Greenberg W L and Budinger T F 1977 Donner algorithms for reconstruction tomography *Lawrence Berkeley National Laboratory Publication* PUB-214
- Huesman R H, Knittel B L, Mazoyer B M, Coxson P G, Salmeron E M, Klein G J, Reutter B W and Budinger T F 1995 Notes on RFIT: a program for fitting compartment models to region-of-interest dynamic emission tomography data *Lawrence Berkeley National Laboratory Report* LBL-37621
- Huesman R H and Mazoyer B M 1987 Kinetic data analysis with a noisy input function *Phys. Med. Biol.* **32** 1569–79
- Kadrmas D J, Frey E C, Karimi S S and Tsui B M W 1998 Fast implementations of iterative reconstruction-based scatter compensation in fully 3D SPECT reconstruction *Phys. Med. Biol.* **43** 857–73
- Kadrmas D J, Frey E C and Tsui B M W 1997 Analysis of the reconstructibility and noise properties of scattered photons in Tc-99m SPECT *Phys. Med. Biol.* **42** 2493–516
- Kendall M, Stuart A and Ord J K 1987 *Kendall's Advanced Theory of Statistics* 5th edn (New York: Oxford University Press) section 10.5
- Leppo J A, DePuey E G and Johnson L L 1991 A review of cardiac imaging with sestamibi and teboroxime *J. Nucl. Med.* **32** 2012–22
- Links J M, Frank T L and Becker L C 1991 Effect of differential tracer washout during SPECT acquisition *J. Nucl. Med.* **32** 2253–7
- Nakajima K, Taki J, Bunko H, Matsudaira M, Muramori A, Matsunari I, Hisada K and Ichihara T 1991 Dynamic acquisition with a three-headed SPECT system: application to technetium 99m SQ30217 myocardial imaging *J. Nucl. Med.* **32** 1273–7
- Press W H, Flannery B P, Teukolsky S A and Vetterling W T 1988 *Numerical Recipes in C* (Cambridge: Cambridge University Press)
- Pretorius P H, Xia W, King M A, Tsui B M W, Pan T S and Villegas B J 1997 Evaluation of right and left ventricular volume and ejection fraction using a mathematical cardiac torso phantom for gated pool SPECT *J. Nucl. Med.* **30** 1528–34
- Ross S G, Welch A, Gullberg G T and Huesman R H 1997 An investigation into the effect of input function shape and image acquisition interval on estimates of washin for dynamic cardiac SPECT *Phys. Med. Biol.* **42** 2193–213
- Smith A M 1994 Dynamic cardiac SPECT imaging *Doctoral Dissertation* Department of Bioengineering, University of Utah, Salt Lake City
- Smith A M and Gullberg G T 1994 Dynamic cardiac SPECT computer simulations for teboroxime kinetics *IEEE Trans. Nucl. Sci.* **41** 1626–3
- Smith A M, Gullberg G T and Christian P E 1996 Experimental verification of technetium-99m-labeled teboroxime kinetic parameters in the myocardium with dynamic single-photon emission computed tomography: reproducibility, correlation to flow, and susceptibility to extravascular contamination *J. Nucl. Cardiol.* **3** 130–42
- Smith A M, Gullberg G T, Christian P E and Datz F L 1994 Kinetic modeling of teboroxime using dynamic SPECT imaging of a canine model *J. Nucl. Med.* **35** 484–95
- Smith M F, Floyd C E Jr, Jaszczak R J and Coleman R E 1992 Reconstruction of SPECT images using generalized matrix inverses *IEEE Trans. Med. Imaging* **11** 165–75

- Terry J A, Tsui B M W, Perry J R, Hendricks J L and Gullberg G T 1990 The design of a mathematical phantom of the upper human torso for use in 3-D SPECT imaging research *Biomedical Engineering: Opening New Doors, Proc. 1990 Fall Meeting of the Biomedical Engineering Society (Blacksburg, VA)* (New York: New York University Press) pp 1467–74
- Tsui B M W, Zhao X D, Gregoriou G K, Lalush D S, Frey E C, Johnson R E and McCartney W H 1994 Quantitative cardiac SPECT reconstruction with reduced image degradation due to patient anatomy *IEEE Trans. Nucl. Sci.* **41** 2838–44
- Welch A E, Smith A M and Gullberg G T 1995 An investigation of the effect of finite system resolution and photon noise on the bias and precision of dynamic cardiac SPECT parameters *Med. Phys.* **22** 1829–36